

# Binder-free, multidentate bonding-induced carbon nano-oligomer assembly for boosting charge transfer and capacitance of energy nanoparticle-based textile pseudocapacitors

Jeongyeon Ahn<sup>a,1</sup>, Woojae Chang<sup>a,1</sup>, Yongkwon Song<sup>a,1</sup>, Youhyun Son<sup>a</sup>, Yongmin Ko<sup>b,\*</sup>, Jinhan Cho<sup>a,c,d,\*</sup>

<sup>a</sup> Department of Chemical and Biological Engineering, Korea University, 145 Anam-ro, Seongbuk-gu, Seoul 02841, Republic of Korea

<sup>b</sup> Division of Energy Technology, Materials Research Institute, Daegu Gyeongbuk Institute of Science and Technology (DGIST), 333 Techno Jungang-daero, Hyeonpung-eup, Dalseong-gun, Daegu 42988, Republic of Korea

<sup>c</sup> KU-KIST Graduate School of Converging Science and Technology, Korea University, 145 Anam-ro, Seongbuk-gu, Seoul 02841, Republic of Korea

<sup>d</sup> Soft Hybrid Materials Research Center, Advanced Materials Research Division, Korea Institute of Science and Technology (KIST), 5 Hwarang-ro 14-gil, Seongbuk-gu, Seoul 02792, Republic of Korea

## ARTICLE INFO

### Keywords:

Textile pseudocapacitor  
Direct multidentate bonding-induced assembly  
Surface-functionalized carbon nano-oligomer

## ABSTRACT

Energy storage performance of pseudocapacitors (PCs) critically depends on the integration and distribution of electrochemically active materials and conductive fillers as well as the intrinsic energy storage capacity of active materials. This is particularly challenging for nano-sized pseudocapacitive materials that offer high energy density but suffer from low electrical conductivity. Additionally, conventional electrode fabrication methods often neglect crucial interfacial interactions and electrolyte wettability essential for nanoparticle-based PC electrodes in a 3D structure, which can lead to performance degradation. Here, we present a novel approach to fabricate 3D-structured pseudocapacitor electrodes by directly and sequentially assembling hydrophobic energy nanoparticles (NPs) and hydrophilic carbon nano-oligomers (CNOs) with branched space arms onto 3D textile current collectors, eliminating the need of insulating and hydrophobic organic components. This assembly based on direct interfacial multidentate interactions between  $\text{MnO}_x$  NPs and CNOs ensure a uniform nano-level distribution over the entire metallic textile surface. The resulting positive electrodes (i.e.,  $\text{MnO}_x$  NP/CNO-based textiles) exhibit the outstanding areal capacitance of  $\sim 1,725 \text{ mF cm}^{-2}$  at  $5.0 \text{ mA cm}^{-2}$ . This capacitance can be further increased to  $\sim 3,244 \text{ mF cm}^{-2}$  at  $10 \text{ mA cm}^{-2}$  via a multi-stacking method. When paired with negative electrodes (i.e.,  $\text{Fe}_3\text{O}_4$  NP/CNO-based textiles) fabricated using the same approach, asymmetric full-cell demonstrate remarkable areal energy/power densities that surpass those of conventional pseudocapacitors.

## 1. Introduction

Pseudocapacitors (PCs) have emerged as promising energy storage solutions that can bridge the gap between high-power carbon-based electric double-layer capacitors (EDLCs) and high-energy rechargeable batteries [1–6]. These systems are characterized by storing charges through the fast Faradaic processes at or near the surface of the active materials (within the range of ten nanometers from the surface), which do not involve phase transformations. Therefore, reducing the size of the active materials—ideally to the nanoscale—can result in higher energy efficiency and good rate-capabilities [7–10]. That is, the use of

nanomaterials for PCs enables to expand the electrochemically active surface area and minimize the charge transfer distance between adjacent components, thereby further boosting the performance of the electrodes. In this regard, multivalent transition metal oxide nanoparticles (NPs), such as  $\text{MnO}_x$  and  $\text{FeO}_x$ , have received great attention as potential candidates for pseudocapacitive materials due to their high theoretical capacitance originating from multi-electron-mediated oxidation states, as well as their facile tunability into various nanostructures [1–4,7].

Importantly, to fully utilize the advantages of such active NPs, the key consideration is to ensure a uniform and stable distribution within the electrode through the efficient integration of NPs with supporting

\* Corresponding authors.

E-mail addresses: [yongmin.ko@dgist.ac.kr](mailto:yongmin.ko@dgist.ac.kr) (Y. Ko), [jinhan71@korea.ac.kr](mailto:jinhan71@korea.ac.kr) (J. Cho).

<sup>1</sup> These authors contributed equally to this work.

components, such as conductive fillers and binders. Basically, these supporting components play a significant role in facilitating charge transfer within the electrode and/or imparting appropriate surface properties to active materials [11–14], which improves the electrochemical performance as well as the structural integrity. However, conventional mechanical mixing approaches to form an active slurry have much difficulty in effectively meeting the aforementioned requirements, which can become more problematic as the particle size decreases to the order of a few nanometers [12]. The essence of such problems lies in the reliance on simple physical mixing, which neglects complementary interfacial interactions between active NPs and conductive fillers [15,16]. In general, achieving an optimal electrode design for higher energy density involves maximizing the mass ratio of active materials to the other supporting components (*i.e.*, conductive fillers and binders) as much as possible. However, active NPs with extremely large active surface areas not only possess organic ligands which can act as contact resistance within electrodes [17,18], but also require large amounts of polymeric binders to connect adjacent electrode components and/or stabilize the NP interfaces [16,19]. Despite the introduction of these electrochemically inactive organic components (organic ligands and binders), a simple mechanical mixing process is not sufficient to achieve uniform dispersion of active NPs and conductive fillers within the electrode. As a result, this dilemma of active NPs leads to sluggish charge transfer between adjacent active NPs, resulting in a decrease in the electrochemical performance of the electrode [20,21].

Another crucial factor that should not be overlooked is the influence of electrolyte wettability on the electrode components. For example, when assembling the PC electrodes with polar solvents (particularly aqueous electrolytes) for better rate performance, conventional hydrophobic carbon-based conductive fillers (*e.g.*, CNT and/or carbon black) and poly(vinylidene fluoride) binders can impede effective charge transfer between neighboring active components due to the formation of a thick diffusion layer at the electrode/electrolyte interfaces [19,22,23]. In particular, the hydrophobic CNTs with a high-aspect-ratio (typically several hundred micrometers in length) are prone to bundling due to their poor dispersion stability, resulting in uneven charge distribution. Similarly, this feature tends to be more prominent when using nano-sized active materials [24]. Although some studies have utilized the acid treatment method of carbon materials to introduce functional groups for incorporation with active materials, hydrophobic polymeric binders and additional conductive fillers are still required for preparing electrodes [25–27]. To the best of our knowledge, studies on binder-free pseudocapacitor electrodes using surface-modified carbon black assembly have never been reported by other research groups.

In this regard, to fully exploit the size advantage of PC NPs and to control the electrolyte wettability of the electrode components, it is highly important to develop a unique assembly approach that can properly arrange the conductive components at the interfaces between neighboring NPs, while directly connecting them without the presence of insulating and hydrophobic components. Although it has been reported that cationic amine ( $\text{NH}_3^+$ ) or neutral amine ( $\text{NH}_2$ )-functionalized CNTs can also be assembled with active NPs or chemically reduced MnO layer without polymeric binders through electrostatic-bonding layer-by-layer (LbL) assembly, the PC electrodes fabricated from such approaches exhibited relatively low areal energy storage performance due to low loading amounts of adsorbed PC components onto bulky CNTs [28,29]. In particular, given the significance of areal performance (areal capacitance, areal energy density, and areal power density) for the practical utilization of PC devices [30,31], a novel assembly approach is required to ensure uniform and dense deposition of active components over the entire regions, ranging from the interior to the exterior, of 3D porous current collectors with extremely large areal surfaces but complex structures. Addressing these challenges will unlock the full potential of NP-based PC electrodes and pave the way for highly efficient energy storage devices.

In this study, we introduce a conductive linker-based nanoblending

approach of active NPs for developing high-performance binder-free pseudocapacitive textiles. This approach involves the direct and robust assembly of hydrophobic PC NPs with hydrophilic carbon nanoligomers (CNOs) onto 3D textile current collectors, completely eliminating the presence of insulating or hydrophobic organic components within electrode. Initially, hydrophobically aggregated pristine carbon blacks were converted into hydrophilic/conductive CNOs with a size range of 20–30 nm and branched space arms through chemical treatments, granting them high dispersion in polar solvents. These solution-processable CNOs served a dual function, acting as both conductive fillers with branched space arms and multidentate linkers, directly bridging all interfaces within the electrodes without any aid of hydrophobic or hydrophilic polymeric binders. By strategically incorporating functional groups into CNOs, we established a robust multidentate bonding between PC NPs and CNOs. This assembly ensured a uniform distribution of electrode components at the nanoscale without the use of insulating polymeric binders, constructing a more efficient charge transfer network within the electrodes. Importantly, the hydrophilic functional groups of CNOs completely replaced the original hydrophobic organic ligands on the PC NPs, inducing hydrophilic properties throughout the entire electrode. In this regard, we emphasize that our binder-free approach using a robust assembly of interfacial interactions between a few nm-sized PC NPs and CNOs is obviously different from the approaches reported by other research groups.

To further demonstrate the effectiveness of our approach, we utilized oleate ligand-stabilized  $\text{MnO}_x$  NPs (OA- $\text{MnO}_x$  NPs) with a diameter of 8.3 nm as positive/active components in a pseudocapacitor model system. Although the  $\text{MnO}_x$  NPs themselves have high theoretical capacitance values, they seriously suffer from poor electrical conductivity close to insulating properties. However, by using our assembly method with CNOs, we were able to achieve a significant improvement in electrochemical performance, which was entirely due to the assembled CNOs. For this goal, the OA- $\text{MnO}_x$  NPs are sequentially assembled with CNOs onto highly porous Ni textile current collectors (NTCs) fabricated by the metallization of carbonized cotton textiles (CCTs). The resulting positive electrodes (*i.e.*, ( $\text{MnO}_x$  NP/CNO)-based NTCs with a  $\text{MnO}_x$  NP loading mass of  $\sim 5.0 \text{ mg cm}^{-2}$ ) delivered an exceptionally high areal capacitance of  $\sim 1,725 \text{ mF cm}^{-2}$  (at  $5.0 \text{ mA cm}^{-2}$ ). This value could be further enhanced to  $\sim 3,244 \text{ mF cm}^{-2}$  (at  $10 \text{ mA cm}^{-2}$ ) through a multi-stacking method. It should also be noted that the notable enhancement of energy storage performance through multi-stacked textile electrodes is achieved by highly uniform and porous structure of textile electrode. In stark contrast, comparative  $\text{MnO}_x$  slurry-cast NTCs displayed a notably lower areal capacitance of  $\sim 125 \text{ mF cm}^{-2}$  at the same conditions. Furthermore, we also applied our approach to different metal oxide such as negative/active  $\text{Fe}_3\text{O}_4$  NPs to fabricate asymmetric full-cell (AFC) devices composed of the ( $\text{MnO}_x$  NP/CNO)-based NTCs (positive electrodes) and the ( $\text{Fe}_3\text{O}_4$  NP/CNO)-based NTCs (negative electrodes). These AFC devices demonstrated successful operations in both aqueous and polymer-gel electrolytes with impressive areal energy/power densities and rate capabilities. Given the formation of direct/robust interfaces between metal oxide NPs and hydrophilic/conductive CNOs without any insulating organics, we believe that our approach can provide a basis for designing various high-performance energy storage electrodes.

## 2. Results and discussion

### 2.1. Direct multidentate assembly using CNOs

For the preparation of pseudocapacitor electrodes using a direct multidentate assembly, hydrophobic pristine carbon black aggregates were first converted into hydrophilic carboxylic acid (COOH)-modified CNOs with good dispersion stability in ethanol (Fig. 1A and S1A). The pristine carbon black aggregates agglomerated into a lump, whereas the prepared CNOs exhibited a branched morphology consisting of several

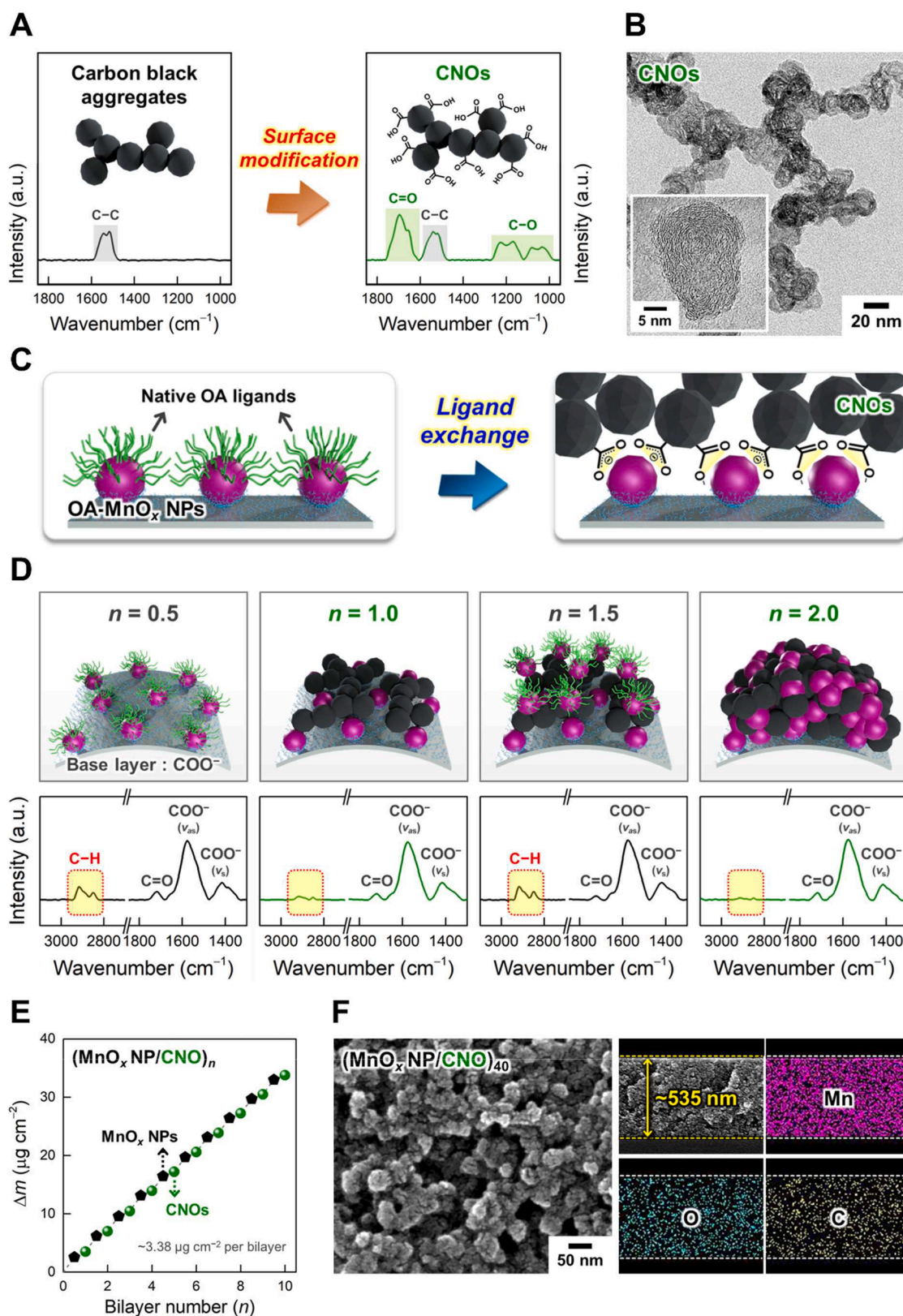


**Fig. 1.** (A) Schematic illustrations and FTIR spectra of pristine carbon black aggregates (left) and surface-modified CNOs (right). (B) HR-TEM images of CNOs (dispersed in ethanol) with a disordered graphite-like crystalline region (inset). (C) Schematic diagrams of an *in-situ* ligand replacement reaction between the multiple COOH groups of CNOs and the native OA ligands on the surface of MnO<sub>x</sub> NPs. (D) FTIR spectra and corresponding schematic representations of (MnO<sub>x</sub> NP/CNO)<sub>n</sub> multilayers as a function of bilayer number ( $n$ ). (E) Mass changes ( $\Delta m$ ) of (MnO<sub>x</sub> NP/CNO)<sub>n</sub> multilayers with increasing the bilayer number ( $n$ ) from 0 to 10 in the QCM analysis. (F) Planar (left) and cross-sectional FE-SEM images with EDS mapping images (right) of the multilayers ( $n = 40$ ).

carbon NPs with diameters of 20–30 nm and a disordered graphite-like crystalline region, which was confirmed by high-resolution transmission electron microscopy (HR-TEM) (Fig. 1B and S1B). The X-ray diffraction (XRD) patterns of the CNOs revealed two broad peaks at  $\sim 24.7$  and  $43.3^\circ$ , corresponding to the graphitic (002) and (100)/(101) planes, which was consistent with those of pristine carbon blacks (Fig. S1C) [32]. The successful formation of multiple COOH groups on the CNO surface was demonstrated by Fourier transform infrared (FTIR) spectra, which showed the appearance of C = O (at  $1,697\text{ cm}^{-1}$ ) and C – O (at  $1,250\text{--}1,000\text{ cm}^{-1}$ ) stretching vibrations, along with the stationary C – C stretching vibration (at  $1,540\text{ cm}^{-1}$ ) of their aromatic rings (see Fig. 1A) [33,34]. In terms of electrical properties, the spin-coated CNO films exhibited a sheet resistance of  $\sim 6.35 \times 10^3\ \Omega\ \text{sq}^{-1}$  at a thickness of  $\sim 240\text{ nm}$ , which was equivalent to an electrical conductivity of  $\sim 6.56\ \text{S cm}^{-1}$ . These results suggested that the CNOs could serve as both conductive fillers and multidentate linkers, directly bridging neighboring metal oxide NPs via multiple COOH groups, while preserving the original physicochemical properties of pristine carbon blacks.

We also synthesized high-energy OA-MnO<sub>x</sub> NPs as positive/active materials to prepare pseudocapacitor electrodes through a direct multidentate assembly with the conductive CNOs. The solvothermally synthesized OA-MnO<sub>x</sub> NPs showed an average diameter of  $\sim 8.3\text{ nm}$  and a well-ordered crystalline phase with good dispersion stability in toluene (Fig. S2). In this case, the bulky OA ligands used to synthesize the MnO<sub>x</sub> NPs ensure high-quality colloidal properties [35,36]; however, these bulky/insulating organics pose a significant barrier to electron transfer between neighboring MnO<sub>x</sub> NPs within the electrodes [36,37]. To overcome this drawback and improve the electron transfer, we induced an *in-situ* ligand replacement reaction that effectively removed the insulating/native OA ligands using direct multidentate interactions between the COOH groups of CNOs and the surface of MnO<sub>x</sub> NPs (Fig. 1C). To better understand these interactions, the FTIR spectra of (MnO<sub>x</sub> NP/CNO)<sub>n</sub> multilayers (here, *n* is bilayer number) were collected during the sequential deposition of OA-MnO<sub>x</sub> NPs and CNOs. During each deposition process, we ensured complete saturation of the component adsorption by carefully controlling the experimental parameters such as concentration and dipping time of the component solutions. Since OA-MnO<sub>x</sub> NPs, unlike CNOs, exhibited prominent C – H stretching vibration (at  $3,000\text{--}2,800\text{ cm}^{-1}$ ) originating from the long alkyl chains of the OA ligands (Fig. S3) [38,39], the ligand replacement was confirmed by the appearance and disappearance of the C – H stretching peak. Specifically, when the OA-MnO<sub>x</sub> NPs were deposited on the outermost surface of the substrates (as indicated by *n* = 0.5 and *n* = 1.5 in Fig. 1D), the C – H stretching peak was obviously detected due to the remaining OA ligands on the upper surface of the MnO<sub>x</sub> NPs. Conversely, the intensity of the C – H stretching peak significantly decreased when the CNOs were subsequently deposited on the MnO<sub>x</sub> NP-coated surface (as indicated by *n* = 1.0 and *n* = 2.0 in Fig. 1D). These contrasting phenomena demonstrated the complete removal of the native OA ligands by the CNOs, which was further supported by the periodic changes in the water contact angles of the multilayers in the assembly process (Fig. S4). In addition, it was worth noting that the multiple COOH groups of CNOs generated the strong bonding with the surface of MnO<sub>x</sub> NPs through the coordination of one or two O atoms in the form of carboxylate ion (COO<sup>−</sup>), which was identified from the asymmetric ( $\nu_{\text{as}}$ ; at  $1,577\text{ cm}^{-1}$ ) and symmetric ( $\nu_{\text{s}}$ ; at  $1,415\text{ cm}^{-1}$ ) COO<sup>−</sup> stretching vibrations in the FTIR spectra (Fig. 1D) [40,41]. That is, the numerous COOH groups of single CNOs could establish stronger direct multidentate interactions with the surface of multiple MnO<sub>x</sub> NPs compared to the monodentate/native OA ligands [39,41]. This superiority enabled the construction of robust pseudocapacitor electrodes without the existence of insulating organic components including polymeric binders and native ligands.

Based on this direct multidentate assembly, we observed the bilayer number-dependent growth behaviors of the (MnO<sub>x</sub> NP/CNO)<sub>n</sub> multilayers by UV–vis spectroscopy (Fig. S5) and quartz crystal microbalance

(QCM) measurements (Fig. 1E). During the alternating deposition of OA-MnO<sub>x</sub> NPs and CNOs, a consistent and uniform growth trends were monitored in the qualitative absorption and quantitative loading mass. When the loading mass ( $\Delta m$ ) was calculated based on the Sauerbrey equation in the QCM analysis, the average  $\Delta m$  per (MnO<sub>x</sub> NP/CNO)<sub>1</sub> bilayer was estimated to be  $\sim 3.38\ \mu\text{g cm}^{-2}$ , with the MnO<sub>x</sub> NPs and CNOs accounting for 75.8 and 24.2 %, respectively. The total film thickness of the multilayers increased linearly from  $\sim 137$  (*n* = 10) to 535 nm (*n* = 40), accompanied by the homogeneous incorporation of CNOs within the MnO<sub>x</sub> NP arrays, as observed in field-emission scanning electron microscopy (FE-SEM) and energy-dispersive X-ray spectroscopy (EDS) mapping images (Fig. 1F and S6). In this case, the mass density of the multilayers was measured to be  $\sim 2.53\ \text{g cm}^{-3}$ , which was a relatively higher than those reported in previous studies for MnO<sub>x</sub>-based electrodes ( $< 1.70\ \text{g cm}^{-3}$ ) [42–44]. Furthermore, it should be noted that our CNO-mediated multidentate assembly could be extended to other metal oxide NPs such as negative/active OA-Fe<sub>3</sub>O<sub>4</sub> NPs (Fig. S7), allowing the construction of asymmetric full-cell devices when paired with the positive (MnO<sub>x</sub> NP/CNO)-based electrodes (more details will be given later).

## 2.2. Pseudocapacitor electrodes using a direct multidentate assembly

After the successful assembly of (MnO<sub>x</sub> NP/CNO)<sub>n</sub> multilayers, we investigated their electrical and electrochemical properties as pseudocapacitor electrodes. For this study, these multilayers were deposited on flat indium tin oxide (ITO) glasses as current collectors (referred to as (MnO<sub>x</sub> NP/CNO)<sub>n</sub> electrodes). First, the electrodes (*n* = 40) exhibited an ohmic conduction mechanism with significantly higher current levels above  $10^{-1}\ \text{mA cm}^{-2}$  compared to spin-coated pristine OA-MnO<sub>x</sub> NP films with insulating properties (current levels of  $\sim 10^{-8}\ \text{mA cm}^{-2}$ ) in two-probe conductivity measurements (see the details in Fig. S8). This result clearly implied that the electron transfer rate could be markedly enhanced by the uniformly distributed CNOs within the MnO<sub>x</sub> NP arrays through a direct multidentate assembly (Fig. 2A).

The electrochemical charge storage capability of (MnO<sub>x</sub> NP/CNO)<sub>n</sub> electrodes was then systematically analyzed using a three-electrode configuration with an aqueous 0.5 M Na<sub>2</sub>SO<sub>4</sub> electrolyte in the potential range of 0 to 0.8 V (vs. Ag/AgCl). When cyclic voltammetry (CV) scans were conducted at  $100\ \text{mV s}^{-1}$ , the current responses increased proportionally with increasing the bilayer number (or loading mass) from 10 to 40 (Fig. 2B). In this case, the total charge density obtained from the integrated CV area showed a linear increase according to the bilayer number (Fig. 2C), suggesting that the electrode capacitance could be further enhanced by simply adjusting the bilayer number. Notably, despite the Faradaic reactions of MnO<sub>x</sub> NPs, the electrodes exhibited quasi-rectangular CV shapes like an electric double-layer capacitance (EDLC) behavior. This charge storage mechanism could be driven by the rapid and sequential multiple surface redox reactions of MnO<sub>x</sub> NPs, specifically involving the surface adsorption of electrolyte cations (*i.e.*, Na<sup>+</sup>) and the incorporation of protons [MnO<sub>x</sub> + *x*Na<sup>+</sup> + *y*H<sup>+</sup> + (*x* + *y*)e<sup>−</sup> → MnO<sub>*x*−1</sub>ONa<sub>*x*</sub>H<sub>*y*</sub>] [45]. Additionally, considering that the EDLC characteristics of the CNOs displayed a negligible CV area (Fig. S9), it could be reasonably concluded that the capacitive behaviors of the electrodes were mainly governed by the high-energy MnO<sub>x</sub> NPs rather than the CNOs. The scan rate-dependent CV curves of the electrodes were also shown in Fig. S10. Although the CV curves became closer to spindle-like shapes with increasing the scan rate due to the polarization effect with increasing the scan rate [46], their overall shapes were maintained without significant distortion even at the high scan rate of  $300\ \text{mV s}^{-1}$ . To gain a deeper understanding of charge storage kinetics, we quantitatively separated the capacitive- and diffusion-controlled currents in the scan rate-dependent CV curves for the electrodes (*n* = 40) based on the Dunn's method using a following equation [7]:

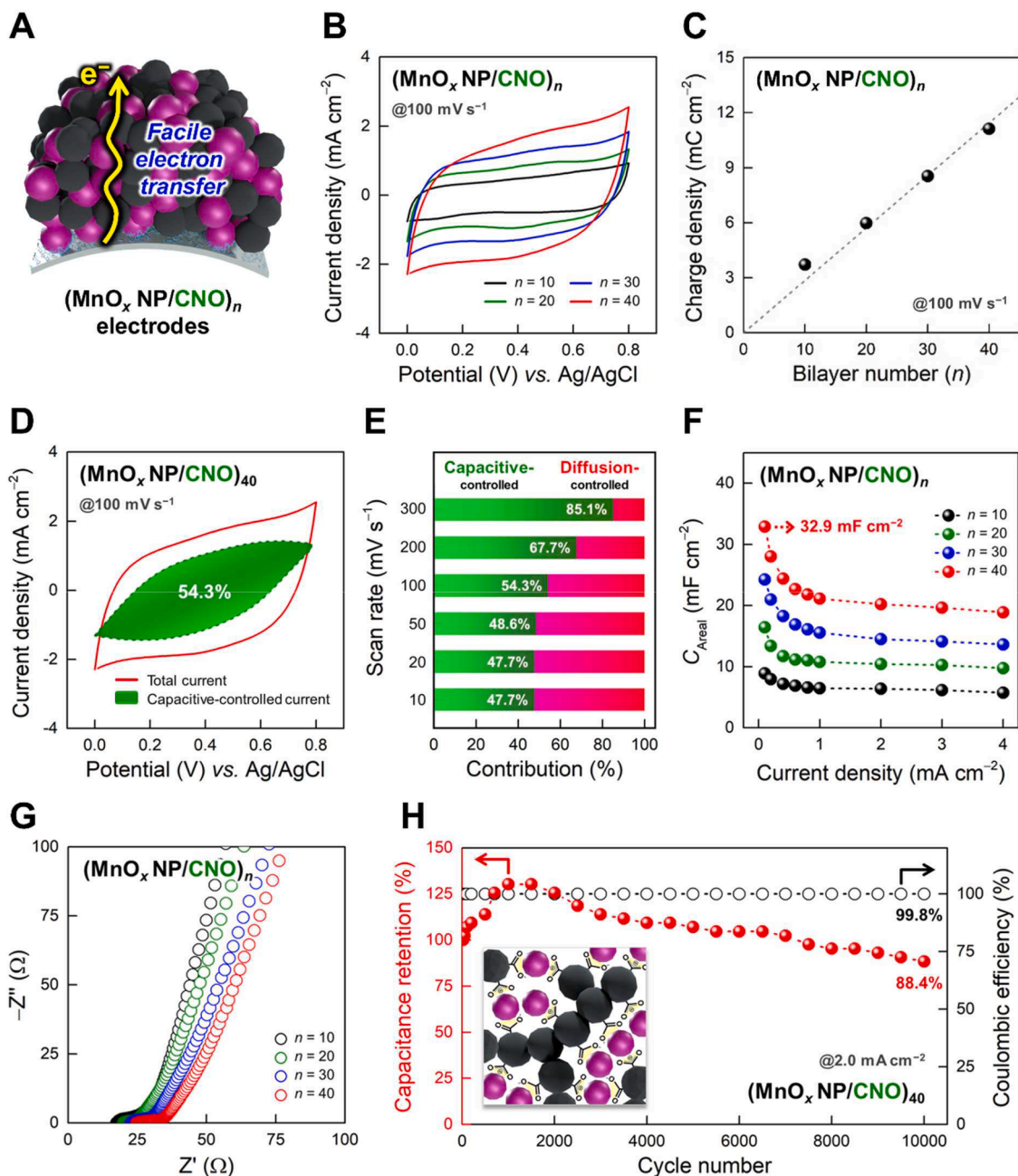


**Fig. 2.** (A) Schematic illustrations of  $(\text{MnO}_x \text{ NP/CNO})_n$  electrodes with enhanced charge transfer kinetics. (B) CV curves and (C) corresponding total charge density of  $(\text{MnO}_x \text{ NP/CNO})_n$  electrodes at  $100 \text{ mV s}^{-1}$  with increasing the bilayer number ( $n$ ) from 10 to 40. (D) Capacitive-controlled currents in the CV curve of the electrodes ( $n = 40$ ) at  $100 \text{ mV s}^{-1}$ . (E) Relative contribution ratios between capacitive- (green bars) and diffusion- (red bars) controlled charge storage of the electrodes ( $n = 40$ ) at different scan rates in the range of 10 to  $300 \text{ mV s}^{-1}$ . (F) Areal capacitance ( $C_{\text{Areal}}$ ) values at various current densities in the range of 0.1 to  $4.0 \text{ mA cm}^{-2}$  and (G) Nyquist plots of  $(\text{MnO}_x \text{ NP/CNO})_n$  electrodes as a function of bilayer number. (H) Capacitance retention (left axis) and Coulombic efficiency (right axis) of the electrodes ( $n = 40$ ) during 10,000 GCD cycles at  $2.0 \text{ mA cm}^{-2}$ . The schematic representations (inset) indicate direct multidentate interactions between  $\text{MnO}_x$  NPs and CNOs, allowing the stable electrochemical operation.

$$i(V) = k_1(v)v + k_2(v)v^{1/2} \quad (1)$$

where  $i(V)$  is the current at a certain potential ( $V$ ), involving the capacitive- ( $k_1v$ ) and diffusion- ( $k_2v^{1/2}$ ) controlled currents at the scan rate ( $v$ ). As a result, the capacitive-controlled contribution was measured to be  $\sim 47.7\%$  at  $10 \text{ mV s}^{-1}$  and gradually increased to  $\sim 85.1\%$  at  $300 \text{ mV s}^{-1}$  (Fig. 2D and 2E). This phenomenon implied that the electrochemically accessible surface, mainly determined by the electrode structure, played a more dominant role in the charge storage (or capacitance) with increasing the scan rate [47].

To obtain the capacitance values of the  $(\text{MnO}_x \text{ NP/CNO})_n$  electrodes,

we performed galvanostatic charge/discharge (GCD) with increasing the current density from 0.1 to  $4.0 \text{ mA cm}^{-2}$  (Fig. S11). In this case, the GCD curves displayed quasi-triangular shapes and much longer charge/discharge times with increasing the bilayer number, which was consistent with the observations in the aforementioned CV curves with an EDLC-like behavior. The electrodes ( $n = 40$ ) exhibited a maximum areal capacitance of  $\sim 32.9 \text{ mF cm}^{-2}$  at  $0.1 \text{ mA cm}^{-2}$  while retaining  $\sim 57.4\%$  of their initial value even at  $4.0 \text{ mA cm}^{-2}$  (Fig. 2F). When the specific and volumetric capacitance values were calculated on the basis of the total loading mass and film thickness of the electrodes, they were measured to be  $\sim 243 \text{ F g}^{-1}$  ( $\sim 321 \text{ F g}^{-1}$  based on the loading mass of

only  $\text{MnO}_x$  NPs) and  $\sim 615 \text{ F cm}^{-3}$ , respectively (Fig. S12). The excellent rate capability of the  $(\text{MnO}_x \text{ NP/CNO})_n$  electrodes was further clarified by electrochemical impedance spectroscopy (EIS) in the frequency range of  $10^5$  to  $0.1 \text{ Hz}$  (Fig. 2G). When the bilayer number increased from 10 to 40, the electrodes showed only slight increments in charge transfer resistance ( $R_{ct}$ ; as observed from the extending semicircles in the high-frequency region) and ion diffusion resistance (as observed from the declining slopes of the tails in the low-frequency region). That is, despite a substantial increase in the loading mass (or film thickness) of poorly conductive  $\text{MnO}_x$  NPs, the observed resistance behaviors verified the efficient charge transfer in the electrodes, which was mainly achieved by the interconnected conductive network of uniformly distributed CNOs. It was also worth noting that the multidentate bonding-induced CNOs enabled robust structural integrity through strong interfacial interactions between the  $\text{MnO}_x$  NPs and the CNOs. The electrodes ( $n = 40$ ) exhibited a long-term operational stability of  $\sim 88.4 \%$  relative to their initial value with a high Coulombic efficiency of  $\sim 99.8 \%$  after 10,000 GCD cycles at  $2.0 \text{ mA cm}^{-2}$  (Fig. 2H). In addition, the capacity retention of above  $100 \%$  at the beginning of GCD cycling was caused by an increase in the electrochemically accessible surface area between  $\text{MnO}_x$  NPs and electrolytes within the electrodes [48].

### 2.3. Pseudocapacitive textile using a direct multidentate assembly

Building on the promising charge storage of  $(\text{MnO}_x \text{ NP/CNO})_n$  electrodes, we extended our direct multidentate assembly to 3D porous current collectors to dramatically enhance their areal performance levels (Fig. 3A). The use of porous current collectors allows for a significant increase in the loading mass of active components without compromising charge transport, a typical issue associated with thickened electrode layers. To exploit this potential advantage, we prepared Ni textile current collectors (NTCs) by using the metallization of CCTs (Fig. S13). During this preparation process, a thin Ni layer of  $\sim 210 \text{ nm}$  was uniformly electrodeposited on the carbonized surface of all individual fibrils without disturbing the porous structure of the textiles (Fig. S14 and S15). More importantly, although the total surface area of the NTCs inevitably decreased with the electrodeposition of the Ni layer (Fig. S16), the NTCs showed a prominent improvement in electrical conductivity by three orders of magnitude. That is, the NTCs showed an extremely low sheet resistance of  $\sim 2.80 \times 10^{-2} \Omega \text{ sq}^{-1}$ , which was in stark contrast to the CCTs with a sheet resistance range from 20 to  $40 \Omega \text{ sq}^{-1}$ . These structural and electrical benefits of the NTCs as 3D porous current collectors could lead to notably improved electrochemical performance compared to when using the CCTs (*more details will be given later*).

Additionally, our 3D porous  $660 \mu\text{m}$ -thick NTCs exhibited much higher specific surface area ( $\sim 0.275 \text{ m}^2 \text{ g}^{-1}$ ) than 3D porous Ni foams ( $\sim 0.035 \text{ m}^2 \text{ g}^{-1}$  at a thickness of  $1,600 \mu\text{m}$ ) and 2D flat Ni foils ( $\sim 0.006 \text{ m}^2 \text{ g}^{-1}$  at a thickness of  $20 \mu\text{m}$ ), as determined by mercury intrusion porosimetry (MIP) measurements and geometric calculations. The significantly higher specific surface area of the porous NTCs compared to the porous Ni foams could be supported by a denser and more compact porous network with smaller pores, as also easily observed in the same magnified FE-SEM images (Fig. 3B). As a result of this increased surface area of the NTCs, when the  $(\text{MnO}_x \text{ NP/CNO})_n$  multilayers were incorporated into the current collectors, the loading mass of  $\text{MnO}_x$  NPs on the NTCs increased by more than  $\sim 97$  times compared to that on the Ni foils at the same bilayer number (Fig. S17). In addition, the FE-SEM and EDS mapping images clearly represented that the  $(\text{MnO}_x \text{ NP/CNO})_{20}$  multilayer-coated NTCs (*i.e.*,  $(\text{MnO}_x \text{ NP/CNO})$ -NTCs) exhibited a conformal coating on all inner/outer Ni fibrils without any notable aggregates (Fig. 3C and S18). Despite the high loading mass of  $\text{MnO}_x$  NPs ( $\sim 5.0 \text{ mg cm}^{-2}$ ), their textile structure with numerous pores was successfully preserved to ensure efficient ion transport. For the comparison with conventional methods, we additionally prepared  $\text{MnO}_x$  slurry-coated NTCs (*i.e.*,  $(\text{MnO}_x \text{ slurry})$ -NTCs) using the physical

blending of commercial  $\text{MnO}_2$  powder, pristine carbon blacks, and COOH group-containing poly(acrylic acid) (PAA) binder at a weight ratio of 8:1:1. However, the highly concentrated and viscous slurries resulted in an uneven morphology with pore clogging and agglomeration within the NTCs, preventing the effective utilization of the porous structure (Fig. 3D).

As expected from the uniformity of the electrodes, the overall performance of the  $(\text{MnO}_x \text{ NP/CNO})$ -NTCs significantly exceeded that of the  $(\text{MnO}_x \text{ slurry})$ -NTCs. For this investigation, electrochemical tests were performed for each electrode with the same loading of active  $\text{MnO}_x$  ( $\sim 5.0 \text{ mg cm}^{-2}$ ) and the increased concentration ( $1.0 \text{ M}$ ) of a  $\text{Na}_2\text{SO}_4$  electrolyte, considering the substantial difference in active surface area between porous and flat electrodes. As shown in the scan rate-dependent CV curves (Fig. 3E and S19), the  $(\text{MnO}_x \text{ NP/CNO})$ -NTCs exhibited more desirable capacitive characteristics with larger CV area compared to the  $(\text{MnO}_x \text{ slurry})$ -NTCs. This large difference in the current responses of the CV curves between the  $(\text{MnO}_x \text{ NP/CNO})$  and  $(\text{MnO}_x \text{ slurry})$  electrode layers was similarly confirmed when using 2D flat ITO current collectors (Fig. S20). Meanwhile, the slight electrochemical deviation from the quasi-rectangular CV shapes (observed in the flat electrodes; Fig. 2B) was caused by the significantly increased loading mass of the poorly conductive  $\text{MnO}_x$  NPs. Additionally, as evidenced from the difference with the CV area of bare NTCs, the overall capacitance was mainly contributed by the electrode layer composed of  $\text{MnO}_x$  NPs rather than the underlying NTCs. Furthermore, the EIS measurements showed that the  $(\text{MnO}_x \text{ NP/CNO})$ -NTCs possessed considerably faster charge transfer kinetics ( $R_{ct}$  of  $\sim 2.4 \Omega$ ) than the  $(\text{MnO}_x \text{ slurry})$ -NTCs ( $R_{ct}$  of  $\sim 102 \Omega$ ) through the fitting using a Randle circuit model (Fig. 3F and S21). Due to this favorable charge transfer network, the  $(\text{MnO}_x \text{ NP/CNO})$ -NTCs provided an unprecedented areal capacitance of  $\sim 1,725 \text{ mF cm}^{-2}$  at  $5.0 \text{ mA cm}^{-2}$  ( $1.0 \text{ A g}^{-1}$ ) with a capacity retention of  $\sim 31.1 \%$  ( $\sim 537 \text{ mF cm}^{-2}$ ) even at the high current density of  $30 \text{ mA cm}^{-2}$  ( $6.0 \text{ A g}^{-1}$ ) (Fig. 3G and S22). On the other hand, the  $(\text{MnO}_x \text{ slurry})$ -NTCs yielded a remarkably low value of  $\sim 125 \text{ mF cm}^{-2}$  at  $5.0 \text{ mA cm}^{-2}$  and a nearly negligible value at  $30 \text{ mA cm}^{-2}$ . This stark difference in performance levels evidently implied that our direct multidentate assembly fully exploited the structural benefits of 3D porous NTCs with a large surface area by providing the uniform nano-level deposition of the components. To further clarify the electrical benefits of the NTCs as 3D porous current collectors, we also compared the electrochemical characteristics of the  $(\text{MnO}_x \text{ NP/CNO})$ -NTCs with the CCT-based electrodes with the same loading mass of electrode layers (Fig. S23). As a result, the NTC-based electrodes exhibited much lower equivalent series resistance (ESR) value than the CCT-based electrodes, resulting a large performance difference in terms of capacitance and rate capability. This indicated that the superior electrical properties of the 3D porous NTCs could contribute to a notable improvement in electrochemical performance. In addition, the electrochemical cycling stability of the  $(\text{MnO}_x \text{ NP/CNO})$ -NTCs was also evaluated during 5,000 GCD cycles at  $30 \text{ mA cm}^{-2}$ , resulting in a satisfactory retention of  $\sim 69.6 \%$  with a Coulombic efficiency of  $\sim 99.8 \%$  (Fig. S24).

Another important aspect of the use of 3D porous NTCs is the potential enhancement of areal performance levels through a multi-stacking method (Fig. 3H). Since the porous NTCs had a well-established charge transfer network based on their interconnected Ni fibrils and numerous pores, the  $(\text{MnO}_x \text{ NP/CNO})$ -NTCs maintained their charge storage capability even in the multi-stacked state. Specifically, the two-stacked  $(\text{MnO}_x \text{ NP/CNO})$ -NTCs showed an approximately twice the CV area of the single-stacked configuration, which was consistent with the increase in the loading mass of  $\text{MnO}_x$  NPs ( $\sim 10 \text{ mg cm}^{-2}$ ) upon stacking (Fig. S25A). In addition, the two-stacked  $(\text{MnO}_x \text{ NP/CNO})$ -NTCs exhibited stable shapes during successive CV sweeps without notable deviations compared to the single-stacked configuration in the same range of scan rates from 10 to  $300 \text{ mV s}^{-1}$  (Fig. S25B and S19A). The areal capacitance value of the two-stacked electrodes could be increased to  $\sim 3,244$  (at  $1.0 \text{ A g}^{-1}$ ) and  $1,093 \text{ mF cm}^{-2}$  (at  $6.0 \text{ A g}^{-1}$ )

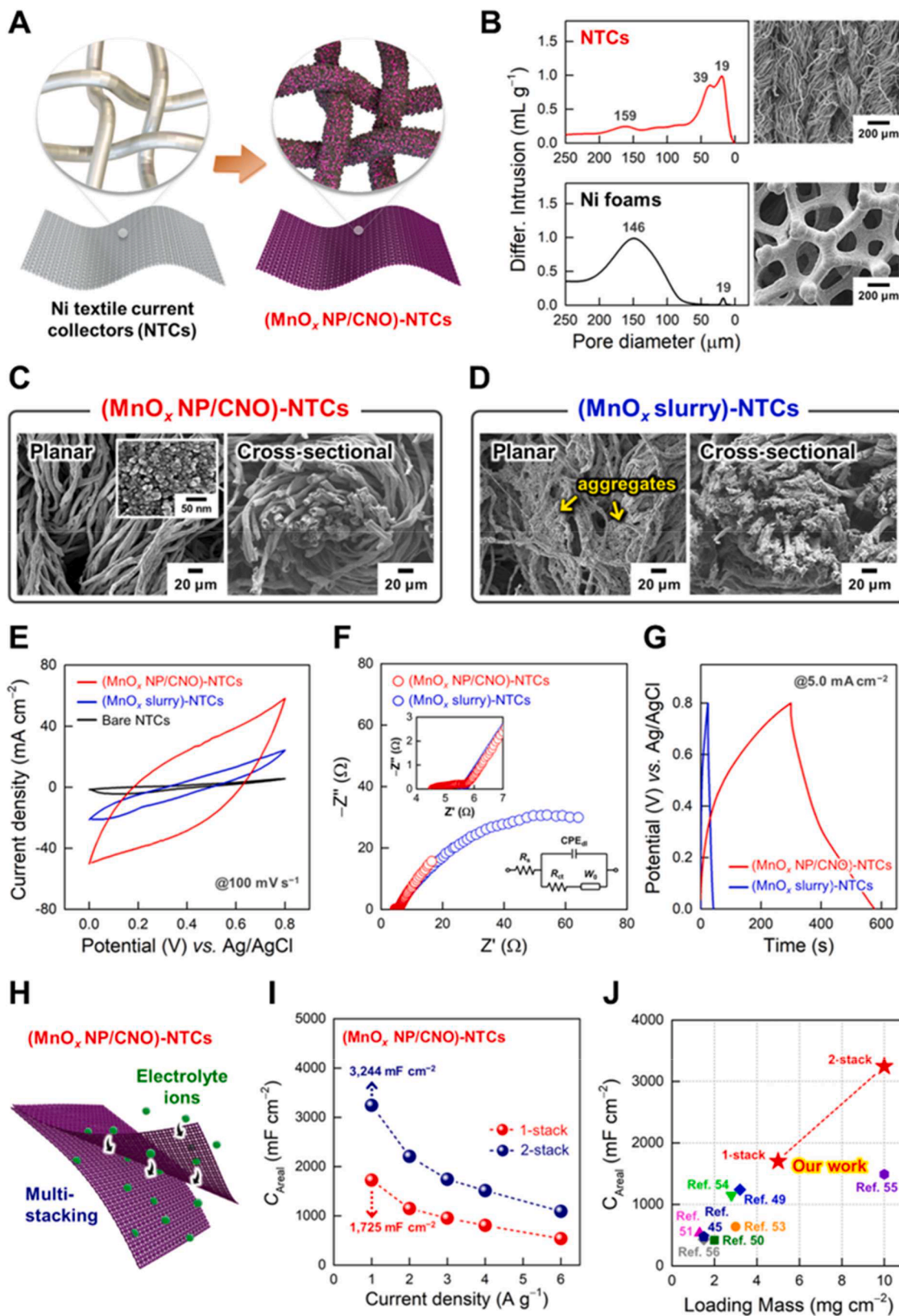


**Fig. 3.** (A) Schematic illustrations of 3D porous NTCs and (MnO<sub>x</sub> NP/CNO)-NTCs. (B) MIP analysis (left) and the same-magnified FE-SEM images (right) for 3D porous NTCs (top) and Ni foams (bottom). Planar and cross-sectional FE-SEM images of (C) (MnO<sub>x</sub> NP/CNO)-NTCs and (D) (MnO<sub>x</sub> slurry)-NTCs. Comparison of (E) CV curves at 100 mV s<sup>-1</sup>, (F) Nyquist plots (with a Randles circuit model for fitting; inset), and (G) GCD curves at 5.0 mA cm<sup>-2</sup> between (MnO<sub>x</sub> NP/CNO)-NTCs and (MnO<sub>x</sub> slurry)-NTCs. (H) Schematic diagrams of multi-stacked (MnO<sub>x</sub> NP/CNO)-NTCs with efficient ion transport. (I) Comparison of areal capacitance (C<sub>Areal</sub>) values between non-stacked and two-stacked (MnO<sub>x</sub> NP/CNO)-NTCs at different current densities in the range of 1.0 to 6.0 A g<sup>-1</sup>. (J) Comparison plots for the loading mass (of active MnO<sub>x</sub> materials) and areal capacitance (C<sub>Areal</sub>) of our work with other literatures.

(Fig. 3I and S26), outperforming the values reported in other studies using active  $\text{MnO}_x$  materials (Fig. 3J and Table S1) [49–56]. Furthermore, the areal capacitance could be increased up to  $\sim 4,523 \text{ mF cm}^{-2}$  (at  $1.0 \text{ A g}^{-1}$ ) with additional stacking (3-stack); however, the increase in the total electrode thickness by the multi-stacking process resulted in an increase in the overall ion diffusion length, leading to a slight decrease in the specific capacitance and rate capability of the ( $\text{MnO}_x$  NP/CNO)-NTCs (Fig. S27). That is, our approach allowed a remarkable enhancement in the areal capacitance (or loading mass) of the electrodes through the effective utilization of 3D porous current collectors with a multi-stacking method, without experiencing performance degradation caused by thickened electrode layers.

#### 2.4. Asymmetric full-cell devices using pseudocapacitive textile

To further demonstrate the practical application of ( $\text{MnO}_x$  NP/CNO)-NTCs, we constructed an asymmetric full-cell (AFC) devices using a  $1.0 \text{ M Na}_2\text{SO}_4$  electrolyte (for aqueous AFCs) and a  $\text{Na}_2\text{SO}_4/\text{PVA}$  gel electrolyte (for solid-state AFCs), as illustrated in Fig. 4A. In particular, our approach could become a versatile platform assembly, which was

applicable not only to  $\text{MnO}_x$  NPs but also to other metal oxide NPs. Thus, we fabricated pseudocapacitor electrodes using negative/active  $\text{Fe}_3\text{O}_4$  NPs through the same CNO-mediated multidentate assembly on porous NTCs, which were paired with the ( $\text{MnO}_x$  NP/CNO)-NTCs in the AFC devices. Similar to the case of using  $\text{MnO}_x$  NPs, the ( $\text{Fe}_3\text{O}_4$  NP/CNO)-NTCs exhibited a homogeneous coating over all Ni fibrils from the exterior to the interior region within the NTCs due to the favorable interfacial affinities between  $\text{Fe}_3\text{O}_4$  NPs and CNOs (Fig. S28). In a half-cell configuration, the as-prepared ( $\text{Fe}_3\text{O}_4$  NP/CNO)-NTCs with a  $\text{Fe}_3\text{O}_4$  NP loading mass of  $\sim 5.0 \text{ mg cm}^{-2}$  exhibited an electrochemically stable behavior in scan rate-dependent CV and current density-dependent GCD tests in the potential range of  $-0.8$  to  $0 \text{ V}$  (vs.  $\text{Ag}/\text{AgCl}$ ), resulting in an areal capacitance of  $\sim 1,062 \text{ mF cm}^{-2}$  (Fig. S29). Then, the total stored charge of the negative ( $\text{Fe}_3\text{O}_4$  NP/CNO)-NTCs was equally balanced with that of the positive ( $\text{MnO}_x$  NP/CNO)-NTCs by adjusting their active area to achieve the best performance in the AFC devices (Fig. 4B). In this case, the optimal area ratio between the positive and negative electrodes was determined to be 1:1.3 based on the surrounded CV area at  $100 \text{ mV s}^{-1}$ .

Based on these results, we assembled the negative ( $\text{Fe}_3\text{O}_4$  NP/CNO)-

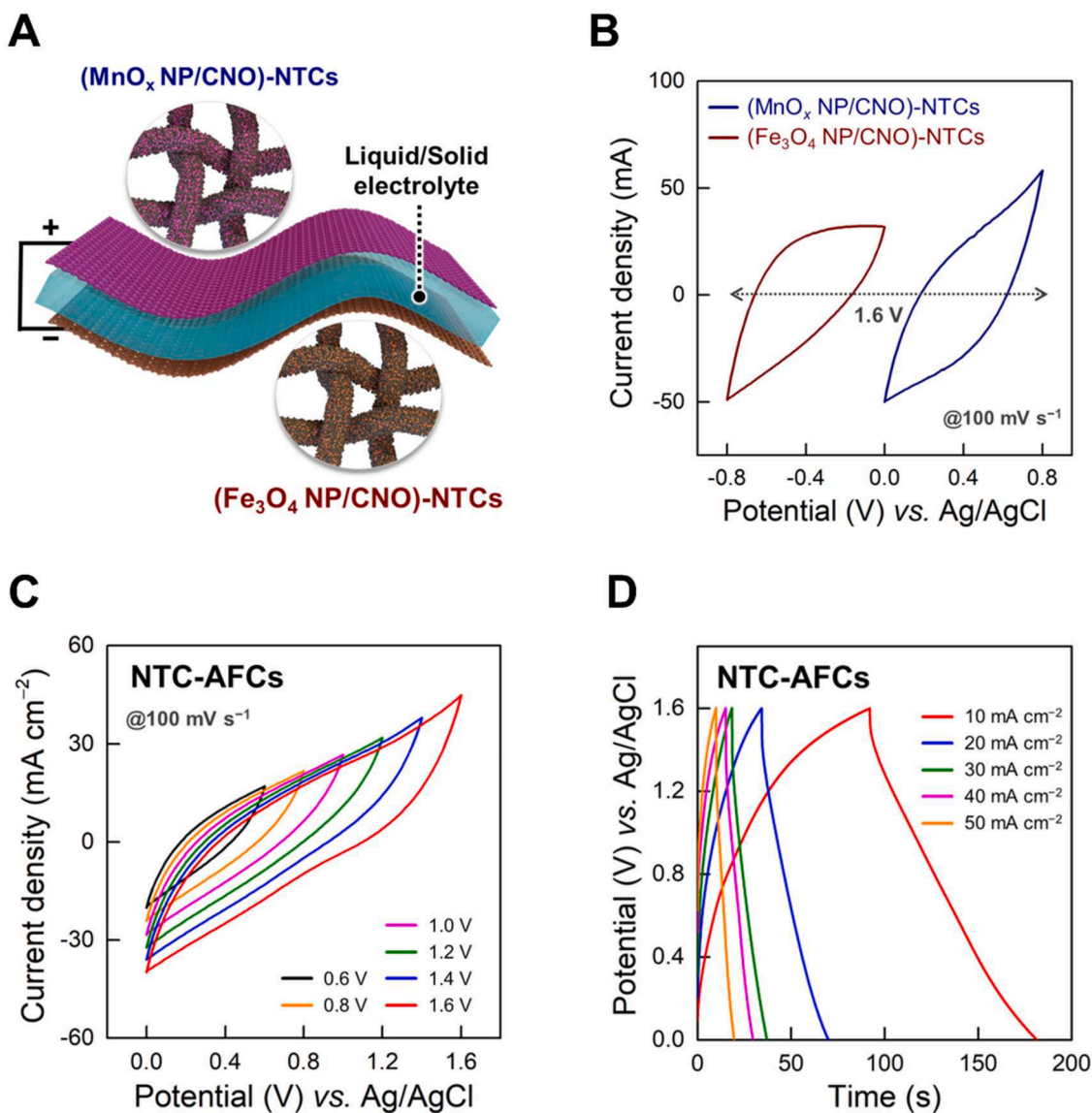


Fig. 4. (A) Schematic illustrations of the NTC-AFCs with positive ( $\text{MnO}_x$  NP/CNO)-NTCs and negative ( $\text{Fe}_3\text{O}_4$  NP/CNO)-NTCs. (B) CV curves of positive ( $\text{MnO}_x$  NP/CNO)-NTCs and negative ( $\text{Fe}_3\text{O}_4$  NP/CNO)-NTCs within the potential window of 0 to 0.8 V and 0 to  $-0.8 \text{ V}$ , respectively, at  $100 \text{ mV s}^{-1}$ . (C) CV curves with extending the voltage window from 0.6 to 1.6 V at  $100 \text{ mV s}^{-1}$  and (D) current density-dependent GCD profiles (in the range of 10 to  $50 \text{ mA cm}^{-2}$ ) of NTC-AFCs.

NTCs with the positive ( $\text{MnO}_x$  NP/CNO)-NTCs to build the NTC-based AFC devices (*i.e.*, NTC-AFCs). As shown in Fig. 4C, the potential window of the NTC-AFCs could be successfully extended to 1.6 V at 100  $\text{mV s}^{-1}$  without any irreversible reactions. Particularly, considering that the potential window beyond 1.6 V may lead to the occurrence of the oxygen evolution reaction (OER) in aqueous electrolytes [47], we selected the optimal potential window of 1.6 V for further electrochemical analysis. In this potential window, the NTC-AFCs exhibited quasi-rectangular CV shapes without undergoing notable distortion in the range of scan rates from 10 to 300  $\text{mV s}^{-1}$  (Fig. S30). The GCD tests of the NTC-AFCs also revealed quasi-triangular and symmetric shapes in the range of current densities from 10 to 50  $\text{mA cm}^{-2}$  (Fig. 4D). These observations clearly demonstrated the good electrochemical reversibility and fast charge/discharge rates of the NTC-AFCs. When the areal capacitance was calculated from the GCD profiles based on the active area of the positive electrodes, it was determined to be  $\sim 590 \text{ mF cm}^{-2}$  at 10  $\text{mA cm}^{-2}$ , retaining 65.2 % of the initial value even at the high current density of 50  $\text{mA cm}^{-2}$ . In addition, the NTC-AFCs delivered an impressive energy density of  $\sim 188 \text{ } \mu\text{Wh cm}^{-2}$  at a power density of  $\sim 7.6 \text{ mW cm}^{-2}$  and retained an energy density of  $\sim 83.1 \text{ } \mu\text{Wh cm}^{-2}$  even at the high power density of  $\sim 30.8 \text{ mW cm}^{-2}$ . These energy/power performance levels were higher than those recorded in previous literatures, which primarily fabricated the electrodes using conventional slurry casting methods (Table S2). It was also noteworthy that our NTC-AFCs could be successfully operated in an all-solid-state configuration using a  $\text{Na}_2\text{SO}_4/\text{PVA}$  gel electrolyte (Fig. S31A). In this case, the solid-state NTC-AFCs showed a stable electrochemical behavior in successive CV and GCD sweeps (Fig. S31B and S31C), which indicated potential practical applications in a variety of wearable/flexible electronics.

### 3. Conclusion

In conclusion, we introduced a conductive linker-based assembly approach to develop high-performance pseudocapacitive textile by directly integrating PC NPs and conductive CNOs with branched space arms on 3D porous NTCs. In particular, the multiple COOH moieties of CNOs induced an *in-situ* ligand replacement, which effectively removed the inactive/insulating ligands on the surface of PC NPs, thus enabling the direct multidentate bonding assembly of the electrodes based on robust interfacial interactions between the components. Due to this interfacial design, the conductive CNOs with multidentate bonding were homogeneously distributed within the PC NP arrays during the subsequent assembly process, which contributed to the formation of an interconnected charge transfer network. Moreover, our assembly approach could fully exploit the structural advantages of the as-prepared 3D porous NTCs with attractive properties (*i.e.*, metal-like conductivity, large specific surface area, and numerous pores). The resulting positive ( $\text{MnO}_x$  NP/CNO)-NTCs exhibited a notably high areal capacitance of  $\sim 1,725 \text{ mF cm}^{-2}$  (at 5.0  $\text{mA cm}^{-2}$ ), which could be further enhanced to  $\sim 3,244 \text{ mF cm}^{-2}$  (at 10  $\text{mA cm}^{-2}$ ) by multi-stacking. When these electrodes were coupled with the negative ( $\text{Fe}_3\text{O}_4$  NP/CNO)-NTCs, the constructed NTC-AFC devices could be stably operated in both aqueous and polymer-gel electrolytes, exhibiting a maximum areal energy density of  $\sim 188 \text{ } \mu\text{Wh cm}^{-2}$  and a power density of  $\sim 30.8 \text{ mW cm}^{-2}$ . With the deep consideration of the interfacial interaction between adjacent electrode components, we believe that our study can provide an insight for the design of electrochemical electrodes that require the intimate interfaces, optimal distribution, and high loading mass of the components.

### CRedit authorship contribution statement

**Jeongyeon Ahn:** Writing – original draft, Methodology, Investigation, Formal analysis. **Woojae Chang:** Writing – original draft, Investigation, Data curation. **Yongkwon Song:** Writing – original draft, Visualization, Validation, Methodology. **Youhyun Son:** Visualization.

**Yongmin Ko:** Formal analysis, Funding acquisition, Writing – review & editing. **Jinhan Cho:** Conceptualization, Funding acquisition, Methodology, Supervision, Writing – review & editing.

### Declaration of competing interest

The authors declare that they have no known competing financial interests or personal relationships that could have appeared to influence the work reported in this paper.

### Data availability

Data will be made available on request.

### Acknowledgments

This work was supported by the National Research Foundation of Korea (NRF) grant funded by the Korea government (Ministry of Science and ICT) (NRF-2021R1A2C3004151) and by the DGIST R&D Programs of the Ministry of Science and ICT of Korea (24-ET-01). We also acknowledge support from KIST Institutional Program (2V09840–23-P025) and the KU-KIST Graduate School of Converging Science and Technology Program.

### Supplementary materials

Supplementary material associated with this article can be found, in the online version, at doi:10.1016/j.ensm.2024.103396.

### References

- [1] C. Choi, D.S. Ashby, D.M. Butts, R.H. DeBlock, Q. Wei, J. Lau, B. Dunn, Achieving high energy density and high power density with pseudocapacitive materials, *Nat. Rev. Mater.* 5 (2020) 5–19, <https://doi.org/10.1038/s41578-019-0142-z>.
- [2] P. Simon, Y. Gogotsi, Perspectives for electrochemical capacitors and related devices, *Nat. Mater.* 19 (2020) 1151–1163, <https://doi.org/10.1038/s41563-020-0747-z>, 19.
- [3] S. Fleischmann, J.B. Mitchell, R. Wang, C. Zhan, D. Jiang, V. Presser, V. Augustyn, Pseudocapacitance: from fundamental understanding to high power energy storage materials, *Chem. Rev.* 120 (120) (2020) 6738–6782, <https://doi.org/10.1021/acs.chemrev.0c00170>.
- [4] F. Wang, J. Lee, L. Chen, G. Zhang, S. He, J. Han, J. Ahn, J.Y. Cheong, Inspired by wood: thick electrodes for supercapacitor, *ACS Nano* 17 (2023) 8866–8898, <https://doi.org/10.1016/j.joule.2018.09.020>.
- [5] D. Pakulski, A. Gorczynski, W. Czepa, Z. Liu, L. Ortolani, V. Morandi, V. Patroniak, A. Ciesielski, P. Samori, Novel keprate type polyoxometalate-surfactant-graphene hybrids as advanced electrode materials for supercapacitors, *Energy Storage Mater* 17 (2019) 186–193, <https://doi.org/10.1038/energy.2017.105>.
- [6] N. Choudhary, C. Li, J. Moore, N. Nagaiah, L. Zhai, Y. Jung, J. Thomas, Asymmetric supercapacitor electrodes and devices, *Adv. Mater.* 29 (2017) 1605336, <https://doi.org/10.1002/adma.201605336>.
- [7] V. Augustyn, P. Simon, B. Dunn, Pseudocapacitive oxide materials for high-rate electrochemical energy storage, *Energy Environ. Sci.* 7 (2014) 1597–1614, <https://doi.org/10.1039/C3EE44164D>.
- [8] E. Pomerantseva, F. Bonaccorso, X. Feng, Y. Cui, Y. Gogotsi, Energy storage: the future enabled by nanomaterials, *Science* 336 (2019) eaan8285, <https://doi.org/10.1126/science.aan8285>.
- [9] J. Yan, S. Li, B. Lan, Y. Wu, P.S. Lee, Rational design of nanostructured electrode materials toward multifunctional supercapacitors, *Adv. Funct. Mater.* 30 (2020) 1902564, <https://doi.org/10.1002/adfm.201902564>.
- [10] Y. Song, S. Lee, Y. Ko, J. Huh, Y. Kim, B. Yeom, J.H. Moon, J. Cho, Charge-transfer effects of organic ligands on energy storage performance of oxide nanoparticle-based electrodes, *Adv. Funct. Mater.* 32 (2022) 2106438, <https://doi.org/10.1002/adfm.202106438>.
- [11] S. Srivastava, et al., 25th anniversary article: polymer-particle composites: phase stability and applications in electrochemical energy storage, *Adv. Mater.* 26 (2014) 201, <https://doi.org/10.1002/adma.201303070>.
- [12] A. Kraysberg, E.E. Y, Conveying advanced Li-ion battery materials into practice the impact of electrode slurry preparation skills, *Adv. Energy Mater.* 6 (21) (2016) 1600655, <https://doi.org/10.1002/aenm.201600655>.
- [13] A. Saal, T. Hagemann, U.S. Schubert, Polymers for battery applications-active materials, membranes, and binders, *Adv. Energy Mater.* 11 (2020) 2001984, <https://doi.org/10.1002/aenm.202001984>.
- [14] W. Dou, M. Zheng, W. Zhang, T. Liu, F. Wang, G. Wan, Y. Liu, X. Tao, Review on the binders for sustainable high-energy density lithium ion batteries: status, solutions, and prospects, *Adv. Funct. Mater.* 33 (45) (2023) 2302161, <https://doi.org/10.1002/adfm.202305161>.

- [15] J. Jiang, Y. Li, J. Liu, X. Huang, C. Yuan, X.W. Lou, Recent advances in metal oxide-based electrode architecture design for electrochemical energy storage, *Adv. Mater.* 24 (2012) 5166–5180, <https://doi.org/10.1002/adma.201202146>.
- [16] J. Ahn, Y. Song, Y.J. Kim, D. Nam, T. Kim, K. Kwak, C.H. Kwon, Y. Ko, S.J. Lee, J. Cho, Redox-active ligand-mediated assembly for high-performance transition metal oxide nanoparticle-based pseudocapacitors, *Chem. Eng. J.* 455 (2023) 140742, <https://doi.org/10.1016/j.cej.2022.140742>.
- [17] I. Ryu, G. Choe, H. Kwon, D. Hong, S. Yim, Overcoming the trade-off between optical transmittance and areal capacitance of transparent supercapacitors for practical application, *Small* 19 (2023) 2207270, <https://doi.org/10.1002/smll.202207270>.
- [18] M. Sun, Q. Fang, Z. Li, C. Cai, H. Li, B. Cao, W. Shen, T.X. Liu, Y. Fu, Co-precipitation synthesis of CuCo<sub>2</sub>O<sub>4</sub> nanoparticles for supercapacitor electrodes with large specific capacity and high rate capability, *Electrochimica Acta* 397 (2021) 139306, <https://doi.org/10.1016/j.electacta.2021.139306>.
- [19] L. Zhang, X. Qin, S. Zhao, A. Wang, J. Luo, Z.L. Wang, F. Kang, Z. Lin, B. Li, Advanced matrixes for binder-free nanostructured electrodes in lithium-ion batteries, *Adv. Mater.* 32 (2020) 1908445, <https://doi.org/10.1002/adma.201908445>.
- [20] F. Wang, R. Robert, N.A. Chernova, N. Pereira, F. Omenya, F. Badway, X. Hua, M. Ruotolo, R. Zhang, L. Wu, V. Volkov, D. Su, B. Key, M.S. Whittingham, C. P. Grey, G.G. Amatucci, Y. Zhu, J. Graetz, Conversion reaction mechanisms in lithium ion batteries: study of the binary metal fluoride electrodes, *J. Am. Chem. Soc.* 133 (2011) 18828–18836, <https://doi.org/10.1021/ja206268a>.
- [21] Y. Ko, M. Kwon, W.K. Bae, B. Lee, S.W. Lee, J. Cho, Flexible supercapacitor electrodes based on real metal-like cellulose papers, *Nat. Commun.* 8 (2017) 536, <https://doi.org/10.1038/s41467-017-00550-3>.
- [22] Y. Luo, L. Wang, Z. Wei, Q. Huang, Y. Deng, Z. Zheng, Cracking-controlled slurry coating of mosaic electrode for flexible and high-performance lithium-sulfur battery, *Adv. Energy Mater.* 13 (2023) 2203621, <https://doi.org/10.1002/aenm.202203621>.
- [23] Y. Song, W. Bae, J. Ahn, Y. Son, M. Kwon, C.H. Kwon, Y. Kim, Y. Ko, J. Cho, Carbon nanocluster-mediated nanoblending assembly for binder-free energy storage electrodes with high capacities and enhanced charge transfer kinetics, *Adv. Sci.* 10 (2023) 2301248, <https://doi.org/10.1002/adv.202301248>.
- [24] S.H. Park, et al., High areal capacity battery electrodes enabled by segregated nanotube networks, *Nat. Energy* 4 (2019) 560, <https://doi.org/10.1038/s41560-019-0398-y>.
- [25] P. Nikhil, S. Sornambikai, G. Bhuvaneshwari, N. Ponpandian, C. Viswanathan, Functionalized ketjenblack infusion into expanded interlayer spacing of Ti<sub>3</sub>C<sub>2</sub>T<sub>x</sub> MXene nanosheets toward high specific capacitance supercapacitors, *ACS Appl. Electron. Mater.* 5 (2023) 5463–5476, <https://doi.org/10.1021/acsaem.3c00681>.
- [26] D. Zhan P. Xiong, X. Wang, Strongly coupled manganese ferrite/carbon black/polyaniline hybrid for low-cost supercapacitors with high rate capability, *Electrochimica Acta* 185 (2015) 218–228, <https://doi.org/10.1016/j.electacta.2015.10.139>.
- [27] D. Zha, Y. Fu, X. Gao, L. Zhang, X. Wang, Intimately coupled hybrid of carbon black/nickel cobaltite for supercapacitors with enhanced energy-storage properties and ultra-long cycle life, *Electrochimica Acta* 257 (2017) 494–503, <https://doi.org/10.1016/j.electacta.2017.10.104>.
- [28] M.N. Hyder, B.M. Gallang, N.J. Shah, Y. S.-Horn, P.T. Hammond, Synthesis of highly stable sub-8nm TiO<sub>2</sub> nanoparticles and their multilayer electrodes of TiO<sub>2</sub>/MWNT for electrochemical applications, *Nano Lett.* 13 (2013) 4610–4619, <https://doi.org/10.1021/nl401387s>.
- [29] S.W. Lee, J. Kim, S. Chen, P.T. Hammond, Y. S.-Horn, Carbon nanotube/manganese oxide ultrathin film electrodes for electrochemical capacitors, *ACS Nano* 4 (2010) 3889–3896, <https://doi.org/10.1021/nn100681d>.
- [30] W. Chang, D. Nam, S. Lee, Y. Ko, C.H. Kwon, Y. Ko, J. Cho, Fibril-type textile electrodes enabling extremely high areal capacity through pseudocapacitive electroplating onto chalcogenide nanoparticle-encapsulated fibrils, *Adv. Sci.* 9 (2022) 2203800, <https://doi.org/10.1002/adv.202203800>.
- [31] R. Chen, H. Tang, P. He, W. Zhang, Y. Dai, W. Zong, F. Guo, G. He, X. Wang, Interface engineering of biomass-derived carbon used as ultrahigh-energy-density and practical mass-loading supercapacitor electrodes, *Adv. Funct. Mater.* 33 (2023) 2212078, <https://doi.org/10.1002/adfm.202212078>.
- [32] N.R. Ostyn, J.A. Steele, M. De Prins, S.P. Sree, C.V. Chandran, W. Wangermez, G. Vanbutsele, J.W. Seo, M.B.J. Roefsaers, E. Breynaert, J.A. Martens, Low-temperature activation of carbon black by selective photocatalytic oxidation, *Nanoscale Adv.* 1 (2019) 2873–2880, <https://doi.org/10.1039/C9NA00188C>.
- [33] M.C.F. Soares, M.M. Viana, Z.L. Schaefer, V.S. Gangoli, Y. Cheng, V. Caliman, M. S. Wong, G.G. Silva, Surface modification of carbon black nanoparticles by dodecylamine: thermal stability and phase transfer in brine medium, *Carbon N Y* 72 (2014) 287–295, <https://doi.org/10.1016/j.carbon.2014.02.008>.
- [34] E.B. Barros, A.G.S. Filho, V. Lemos, J.M. Filho, S.B. Fagan, M.H. Herbst, J. M. Rosolen, C.A. Luengo, J.G. Huber, Charge transfer effects in acid treated single-wall carbon nanotubes, *Carbon N Y* 43 (2005) 2495–2500, <https://doi.org/10.1016/j.carbon.2005.04.032>.
- [35] J. Park, K. An, Y. Hwang, J.G. Park, H.J. Noh, J.Y. Kim, J.H. Park, N.M. Hwang, T. Hyeon, Ultra-large-scale syntheses of monodisperse nanocrystals, *Nat. Mater.* 3 (2004) 891–895, <https://doi.org/10.1038/nmat1251>.
- [36] Y. Ko, C.H. Kwon, S.W. Lee, J. Cho, Nanoparticle-based electrodes with high charge transfer efficiency through ligand exchange layer-by-layer assembly, *Adv. Mater.* 32 (2020) 2001924, <https://doi.org/10.1002/adma.202001924>.
- [37] J.Y. Kim, N.A. Kotov, Charge transport dilemma of solution-processed nanomaterials, *Chem. Mater.* 26 (2014) 134–152, <https://doi.org/10.1021/cm402675k>.
- [38] K. Yang, H. Peng, Y. Wen, N. Li, Re-examination of characteristic FTIR spectrum of secondary layer in bilayer oleic acid-coated Fe<sub>3</sub>O<sub>4</sub> nanoparticles, *Appl. Surf. Sci.* 256 (2010) 3093–3097, <https://doi.org/10.1016/j.apsusc.2009.11.079>.
- [39] J. Choi, D. Nam, D. Shin, Y. Song, C.H. Kwon, I. Cho, S.W. Lee, J. Cho, Charge-transfer-modulated transparent supercapacitor using multidentate molecular linker and conductive transparent nanoparticle assembly, *ACS Nano* 13 (2019) 12719–12731, <https://doi.org/10.1021/acsnano.9b04594>.
- [40] X. Zhang, L. Chen, L. Yuan, R. Liu, D. Li, X. Liu, G. Ge, Conformation-dependent coordination of carboxylic acids with Fe<sub>3</sub>O<sub>4</sub> nanoparticles studied by ATR-FTIR spectral deconvolution, *Langmuir* 35 (2019) 5770–5778, <https://doi.org/10.1021/acs.langmuir.8b03303>.
- [41] B.C. Mei, K. Susumu, I.L. Medintz, H. Mattoussi, Polyethylene glycol-based bidentate ligands to enhance quantum dot and gold nanoparticle stability in biological media, *Nat. Protoc.* 4 (2009) 412–423, <https://doi.org/10.1038/nprot.2008.243>.
- [42] J.M. Jeong, S.H. Park, H.J. Park, S.B. Jin, S.G. Son, J.M. Moon, H. Suh, B.G. Choi, Alternative-ultrathin assembling of exfoliated manganese dioxide and nitrogen-doped carbon layers for high-mass-loading supercapacitors with outstanding capacitance and impressive rate capability, *Adv. Funct. Mater.* 31 (2021) 2009632, <https://doi.org/10.1002/adfm.202009632>.
- [43] J.A. Pereira, J.N. Lacerda, I.F. Coelho, C.S.C. Nogueira, D.F. Franceschini, E. A. Ponzio, F.B. Mainier, Y. Xing, Tuning the morphology of manganese oxide nanostructures for obtaining both high gravimetric and volumetric capacitance, *Mater. Adv.* 1 (2020) 2433–2442, <https://doi.org/10.1039/D0MA00524J>.
- [44] Y. Ko, D. Shin, B. Koo, S.W. Lee, W.S. Yoon, J. Cho, Ultrathin supercapacitor electrodes with high volumetric capacitance and stability using direct covalent-bonding between pseudocapacitive nanoparticles and conducting materials, *Nano Energy* 12 (2015) 612–625, <https://doi.org/10.1016/j.nanoen.2015.01.002>.
- [45] P. Simon, Y. Gogotsi, Materials for electrochemical capacitors, *Nat. Mater.* 7 (2008) 845–854, <https://doi.org/10.1038/nmat2297>.
- [46] T. Huang, B. Gao, S. Zhao, H. Zhang, X. Li, X. Luo, M. Cao, C. Zhang, S. Luo, Y. Yue, Y. Ma, Y. Gao, All-MXenes zinc ion hybrid micro-supercapacitor with wide voltage window based on V2CTx cathode and Ti3C2Tx anode, *Nano Energy* 111 (2023) 108383, <https://doi.org/10.1016/j.nanoen.2023.108383>.
- [47] J. Zhang, Y. Wang, Y. Qian, H. Jin, X. Tang, Z. Huang, J. Lou, Q. Zhang, Y. Lei, S. Wang, Hierarchical design of cross-linked NiCo<sub>2</sub>S<sub>4</sub> nanowires bridged NiCo-hydroxide polyhedrons for high-performance asymmetric supercapacitor, *Adv. Funct. Mater.* 33 (2023) 2210238, <https://doi.org/10.1002/adfm.202210238>.
- [48] Z.H. Huang, Y. Song, D.Y. Feng, Z. Sun, X. Sun, X.X. Liu, High mass loading MnO<sub>2</sub> with hierarchical nanostructures for supercapacitors, *ACS Nano* 12 (2018) 3557–3567, <https://doi.org/10.1021/acsnano.8b00621>.
- [49] P. Zhao, N. Wang, M. Yao, H. Ren, W. Hu, Hydrothermal electrodeposition incorporated with CVD-polymerisation to tune PPy@MnO<sub>2</sub> interlinked core-shell nanowires on carbon fabric for flexible solid-state asymmetric supercapacitors, *Chem. Eng. J.* 380 (2020) 122488, <https://doi.org/10.1016/j.cej.2019.122488>.
- [50] A. Zhang, R. Zhao, L. Hu, R. Yang, S. Yao, S. Wang, Z. Yang, Y.M. Yan, Adjusting the coordination environment of Mn enhances supercapacitor performance of MnO<sub>2</sub>, *Adv. Energy Mater.* 11 (2021) 2101412, <https://doi.org/10.1002/aenm.202101412>.
- [51] W. Xu, L. Liu, W. Weng, High-performance supercapacitor based on MnO/carbon nanofiber composite in extended potential windows, *Electrochim. Acta* 370 (2021) 137713, <https://doi.org/10.1016/j.electacta.2021.137713>.
- [52] J. Ling, A. Gao, Y. Huang, F. Yi, Q. Li, G. Wang, Y. Liu, D. Shu, Self-templated and triethanolamine-induced hollow MnO<sub>2</sub> nanoboxes with abundant Active Mn<sup>3+</sup> and oxygen vacancies for high-performance Na-ion pseudocapacitors, *Chem. Eng. J.* 452 (2023) 139661, <https://doi.org/10.1016/j.cej.2022.139661>.
- [53] I.H. Oh, S.M. Lee, Y.W. Kim, S. Choi, I. Nam, S.T. Chang, Hydrophobic-barrier-assisted formation of vertically layered capacitive electrodes within a single sheet of paper, *J. Mater. Chem. A* 9 (2021) 27672, <https://doi.org/10.1039/D1TA08854H>.
- [54] Y.H. Liu, Z.Y. Jiang, J.L. Xu, Self-standing metallic mesh with MnO<sub>2</sub> multiscale microstructures for high-capacity flexible transparent energy storage, *ACS Appl. Mater. Interfaces* 11 (2019) 24047–24056, <https://doi.org/10.1021/acsaami.9b05033>.
- [55] C. Wang, J. Huang, Y. Huang, X. Li, W. Zhang, J. Sun, P. Xiong, Y. Fu, L. Xue, J. Zhu, Ligand field regulation of δ-MnO<sub>2</sub> by polyanion modification enables extended potential window in supercapacitors, *J. Power Sources* 581 (2023) 233462, <https://doi.org/10.1016/j.jpowsour.2023.233462>.
- [56] R. Sahoo, D.T. Phan, T.H. Lee, T.H.T. Luu, J. Seok, Y.H. Lee, Redox-driven route for widening voltage window in asymmetric supercapacitor, *ACS Nano* 12 (2018) 8494–8505, <https://doi.org/10.1021/acsnano.8b04040>.